

Measurement of the scintillation time spectra and pulse-shape discrimination of low-energy β and nuclear recoils in liquid argon with DEAP-1

M.G. Boulay,* B. Cai, M. Chen, V.V. Golovko, P. Harvey, R. Mathew, J.J. Lidgard, A.B. McDonald, P. Pasuthip, T. Pollmann, and P. Skensved
*Department of Physics, Engineering Physics, and Astronomy
 Queen's University, Kingston, Ontario, K7L 3N6, Canada*

K. Graham
Department of Physics, Carleton University, Ottawa, Ontario, K1S 5B6, Canada

A.L. Hallin
Department of Physics, University of Alberta, Edmonton, Alberta, T6G 2R3, Canada

D.N. McKinsey, W.H. Lippincott, and J. Nikkel
Department of Physics, Yale University, New Haven, Connecticut, 06520

C.J. Jillings, F. Duncan, and B. Cleveland
*Department of Physics and Astronomy, Laurentian University, Sudbury,
 Ontario, P3E 2C6, and SNOLAB, Lively, Ontario, P3Y 1M3, Canada*

I. Lawson
SNOLAB, Lively, Ontario, P3Y 1M3, Canada

The DEAP-1 low-background liquid argon detector has been used to measure scintillation pulse shapes of β decays and nuclear recoil events and to demonstrate the feasibility of pulse-shape discrimination down to an electron-equivalent energy of 20 keV_{ee}. The relative intensities of singlet/triplet states in liquid argon have been measured as a function of energy between 15 and 500 keV_{ee} for both β and nuclear recoils. Using a triple-coincidence tag we find the fraction of β events that are mis-identified as nuclear recoils to be $< 6 \times 10^{-8}$ between 43–86 keV_{ee} and that the discrimination parameter agrees with a simple analytic model. The discrimination measurement is currently limited by nuclear recoils induced by cosmic-ray generated neutrons, and is expected to improve by operating the detector underground at SNOLAB. The analytic model predicts a β mis-identification fraction of 10^{-10} for an electron-equivalent energy threshold of 20 keV_{ee}. This reduction allows for a sensitive search for spin-independent scattering of WIMPs from 1000 kg of liquid argon with a WIMP-nucleon cross-section sensitivity of 10^{-46} cm².

PACS numbers: 29.00.00, 29.25.-t, 29.40.Mc

I. INTRODUCTION

Separation of β - γ interactions from nuclear recoils is critical for many nuclear and particle astrophysics experiments, including direct searches for dark matter particles. Liquid argon provides very sensitive pulse-shape discrimination based on scintillation timing [1], and it is a favourable target for dark matter particle searches since it can be used to construct a very large target mass detector. In this paper we present results on the pulse-shape discrimination of β - γ events from nuclear recoils with the DEAP-1 liquid argon detector.

Argon has many desirable properties as a scintillator, among them a high light yield of approximately 40 photons per keV [2] and ease of purification so that it can meet the radio-purity requirements of a rare-event search experiment.

Scintillation in argon is a result of the formation of dimers after exposure to ionizing radiation [3]. These occur in singlet and triplet states. On decaying to the ground state, they emit light at a peak wavelength of 128 nm, lower in energy than the lowest excited atomic state [4, 5]. The scintillation light can thus pass through the argon without being absorbed.

The two argon dimer states have vastly different lifetimes, about 6 ns for the singlet and 1.6 μ s for the triplet state [5]. Moreover, the relative population of singlet and triplet states is determined by the linear energy transfer (LET) of the exciting radiation [5], such that fewer triplet excimers are produced at higher LET. With the large difference in lifetimes, the percentage of light signal in the first few tens of nanoseconds is a good estimate for the relative population of the singlet state, allowing for an effective way to discriminate between particles of different LETs, such as low-energy electrons and nuclei.

*Corresponding author, email: mark.boulay@queensu.ca

II. EXPERIMENTAL APPARATUS

The liquid argon cell consists of a stainless steel ultra-high vacuum chamber with two 6-inch diameter glass windows mounted as shown in Fig. 1. The chamber contains a volume of 5.1 L and a mass of 7 kg of liquid argon. All detector components have been selected to minimize radioactivity in the cell, in particular neutrons from (α, n) interactions in detector materials. A $\frac{1}{4}$ -inch thick polymethyl-methacrylate (PMMA) acrylic sleeve coated with TiO_2 is inserted into the target chamber to act as a diffuse reflector and increase scintillation light collection. Scintillation photons in liquid argon have a mean wavelength of 128 nm. Standard vacuum deposition techniques are used to coat the TiO_2 surface of the acrylic sleeve and the inner surfaces of the windows with 0.1 mg/cm^2 of 1,1,4,4-Tetraphenyl-1,3-butadiene (TPB) so as to convert the 128 nm scintillation photons into the visible range for detection by photomultipliers (PMTs). Light from the scintillation cell is transported to the PMTs through 8-inch long PMMA acrylic light guides. To reduce potential backgrounds from Cerenkov radiation generated by cosmic-ray muons, the light guides are constructed of UV-absorbing (UVA) acrylic. The stainless steel scintillation cell and light guides are thermally insulated by multi-layer superinsulation and a vacuum space. The thermal vacuum jacket is supported by a PMMA acrylic vacuum chamber, 12 inches in diameter, as shown in Fig. 1. The inner face of the acrylic light guide rests against the window to the liquid argon cell. The light guides are O-ring sealed to PMMA flanges on the insulating vacuum chamber, and the outer light guide face is at laboratory atmosphere and room temperature. The PMTs are coupled to the light guides with Bicon BC-630 optical gel and operated at room temperature. The light guides serve multiple purposes: to transport visible light from the liquid argon (at 87 K) to the room-temperature PMTs, as the vacuum seal for the insulating chamber, as a thermal barrier between the PMTs and the liquid argon, and to moderate neutrons from the PMTs. The measured heat load in this configuration is approximately 7 watts per light guide.

The target cell is filled with argon that has been purified in the gas phase and then liquefied. The process system consists of a source of ultra-high purity (grade 5) argon gas, a heated Zirconium metal SAES getter [6], and a cooling coil that is immersed in liquid nitrogen. The argon gas at the output of the purification system contains less than 0.1 parts per billion for most impurities. No additional purification of the argon was performed after the detector was filled. The liquid nitrogen is maintained at a constant pressure of approximately 33.5 psia to regulate the temperature of the cryostat. Argon is continuously recirculated through the cooling coil to remove the heat introduced through the acrylic light guides. The results presented here are for 67 days of operation, over which the light yield and detector response were stable (see Fig. 11).

The target chamber is surrounded by a neutron and

γ -ray shield consisting of a minimum of two layers of ultra-pure water in 12-inch cubical polyethylene containers, for a total water shielding thickness of 60 cm. A Geant4 [7, 8] Monte-Carlo simulation showed that the water shield is sufficient to reduce nuclear recoil events in the liquid argon from external-source (α, n) neutrons to less than one per year. The data presented here are from operation of the detector at Queen’s University without any overburden for cosmic-ray shielding. Further data are being collected underground at SNOLAB at a depth of 6000 meters water equivalent. These data will be reported later. At that depth the cosmic-ray muon flux passing through the detector is expected to be less than one per year, reduced from approximately 10 per second at Queen’s.

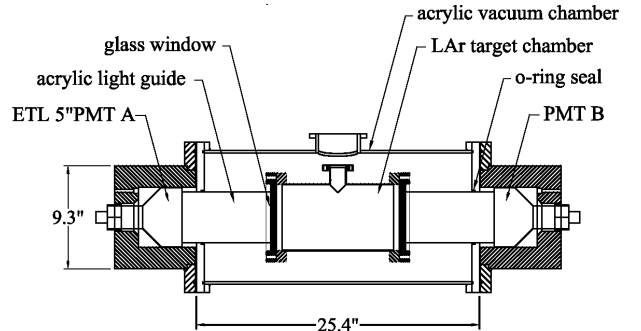


FIG. 1: DEAP-1 detector configuration. Liquid argon is contained in a stainless steel target chamber, which includes an inner acrylic cylinder and a diffuse reflector. Scintillation light from the liquid argon is wavelength-shifted by TPB on the inner detector surface and is transmitted to PMTs operating at room temperature through PMMA acrylic light-guides. The PMTs (5-inch ETL 9390B) are held in place by spring-loaded polyethylene supports, which maintain contact between the PMTs and lightguides.

III. DATA AND ANALYSIS

A. Electronics and Trigger Configurations

Signals from the PMTs are sent to Phillips 778 amplifiers. One output of each amplifier is sent to a LeCroy digitizing oscilloscope that samples the waveforms at 1 GHz for $10 \mu\text{s}$, many times the $1.6 \mu\text{s}$ lifetime of the longest component of scintillation light. The second output of the amplifier is passed to a linear fan-out with one of the two outputs being used for discriminator triggering and the other for more sophisticated triggers. The “DEAP-1” trigger is a signal above discriminator threshold in both PMTs, corresponding to

approximately 1 keV_{ee} , well below the region of interest for this study. The remaining output from the linear fan-out for each PMT is passed to a summing amplifier and then to a shaping amplifier with an integration time of $6 \mu\text{s}$. This summed signal is passed to a single-channel analyzer (SCA) and used as a veto for events far larger in energy than the region of interest. Cutting these high-energy events allows us to increase the effective data-taking rate by a factor of approximately 3. The DEAP-1 trigger with this veto imposed is called the “DEAP-1 SCA trigger”.

The response of DEAP-1 to electromagnetic interactions in the liquid argon is calibrated by a $10 \mu\text{Ci}$ encapsulated ^{22}Na source placed outside of the argon chamber. The source emits a positron and a 1274 keV γ -ray. The positron annihilates in the source container producing back-to-back 511 keV γ -rays. One of the 511 keV γ -rays scatters in the argon, and we use two additional detectors to “tag” the backwards going 511 keV γ ray and the additional 1274 keV γ ray. The source is placed on the axis of an annular NaI detector with dimensions $3.75'' \times 11.5'' \times 12''$ (inner diameter \times outer diameter \times length) to detect the 1274 keV γ -ray. The annulus is divided into 4 sections along its axis with a PMT on each section. The signals from the 4 sections of the annulus are independently amplified (Phillips 778) and discriminated (Phillips 705) with the threshold set just below the 1274 keV peak. The outputs of the discriminators are passed to a logical OR (Phillips 775 with coincidence level 1) to generate the “annulus trigger”. The four annulus sections also have a higher-energy discriminator which is used as a veto on the annulus trigger to reduce backgrounds from cosmic rays.

A cylindrical NaI crystal of dimension $3.25'' \times 3''$ (diameter \times length) coupled to a PMT is placed at one end of the annulus. This PMT signal is amplified and passed to a single-channel amplifier (Ortec 420) which is centered on the 511 keV peak to detect the “backwards” going gamma ray. The “back PMT” trigger is thus generated. The “global tag” is generated when an annulus trigger and a back PMT trigger are coincident. The geometry of this triple-coincidence tag is shown in Fig. 2. The location of the source and back PMT are optimized to maximize the coincidence rate.

Recording with the oscilloscope is triggered by either the DEAP-1 trigger, the DEAP-1 SCA trigger or one of these two triggers in coincidence with the global tag. The timing of the triggers is set such that the leading edge of the trigger is defined by the back PMT so that approximately $1 \mu\text{s}$ of the waveform is recorded before the leading edge of the event. Pulse shape discrimination (PSD) calibration is carried out with the DEAP-1 SCA trigger in coincidence with the global tag.

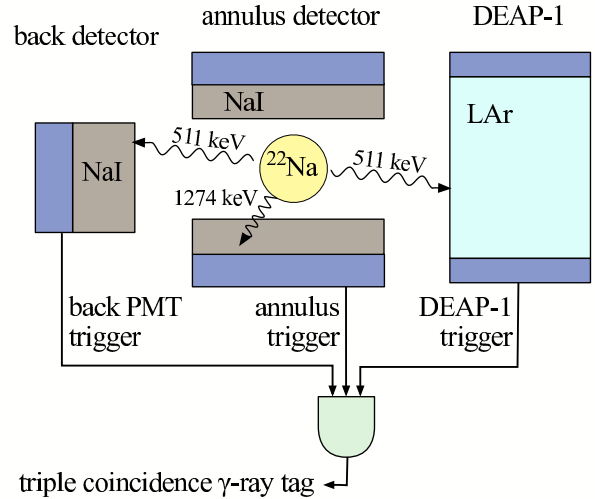


FIG. 2: Calibration source geometry. The decay of ^{22}Na is tagged by γ 's in the back NaI PMT, the annulus detector, and in DEAP-1, which allows a very low non- γ background for calibration of the pulse-shape discrimination.

B. Data Flow

The signal from each PMT is recorded on the oscilloscope at a “high-gain” setting of 50 mV/division . When higher-energy signals are of interest the signals are recorded at both the high-gain setting and a low-gain setting of 500 mV/division on a second channel.

A Linux data-acquisition computer runs an event builder that reads the files in real time and converts them to a ROOT-based [9] format. The root-based data files are automatically transferred to a disk farm on the High-Performance Computing Virtual Laboratory (HPCVL) [10] for offline analysis. For the triple-coincidence calibration, the rate of scattering events in the argon is approximately 10 kHz , the rate of back-PMT and annulus coincidences is approximately 100 Hz , and the triple-coincidence rate is approximately 20 Hz .

C. Analysis

Figure 3 shows PMT traces from a sample γ -ray event in the region of interest from PSD calibration. A linear baseline correction is applied waveform-by-waveform: the baseline is found in the first $0.5 \mu\text{s}$ of the waveform trace. That baseline is used to search for signals above threshold in the final $4 \mu\text{s}$ of the pulse. Areas around these signals are removed and a baseline is calculated at the end of the pulse. A linear function is found from the two baseline regions and subtracted from the total trace.

The leading edge for each signal is found using a voltage threshold of 5 mV , which corresponds to approximately one tenth of a photoelectron. The prompt region of the pulse is defined from 50 ns before the edge to 150

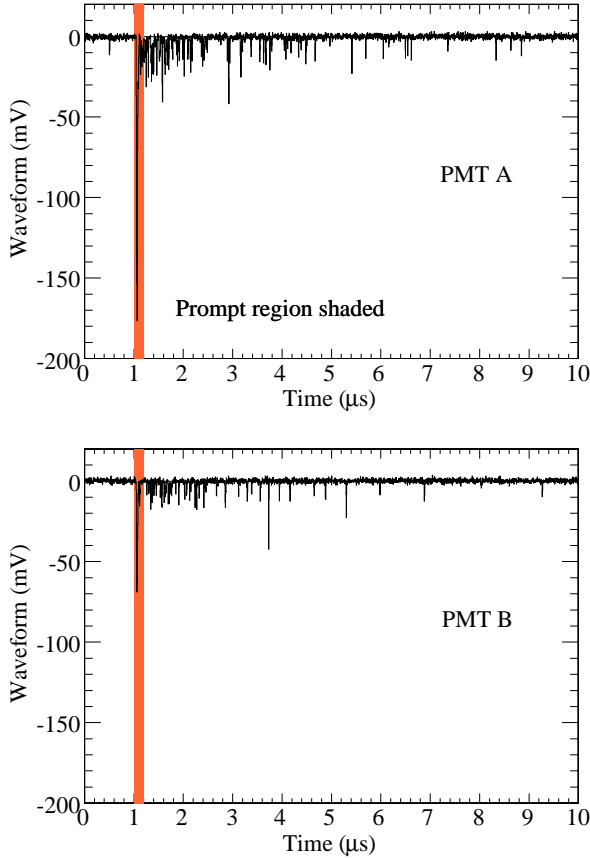


FIG. 3: A sample event from a ^{22}Na PSD calibration run. Shown are the recorded traces for each of the two PMTs, labeled A and B. The shaded area shows the prompt region which begins 50 ns before the leading edge of the pulse and ends 150 ns after the leading edge.

ns after the edge. The late region is defined from 150 ns to the end of the waveform, $\simeq 9 \mu\text{s}$ after the leading edge. The total charge for each PMT for both prompt and late regions is found and converted to units of photoelectrons using the single photoelectron charge calibration described below. Defining $Q_{\text{prompt,late}}^{\text{A,B}}$ as the number of photoelectrons in PMT A or B that are prompt or late, and Total PE as the total number of photoelectrons, we write the fraction of prompt light as

$$F_{\text{prompt}} \equiv \frac{Q_{\text{prompt}}^{\text{A}} + Q_{\text{prompt}}^{\text{B}}}{\text{Total PE}} \quad (1)$$

The relative signals in the two PMTs are used to reconstruct the position of the event, Z_{fit} , along the cylindrical axis of the detector,

$$Z_{\text{fit}} \equiv 35.2 \text{ cm} \times \frac{Q^{\text{A}} - Q^{\text{B}}}{\text{Total PE}}, \quad (2)$$

where $Q^{\text{A,B}} \equiv Q_{\text{prompt}}^{\text{A,B}} + Q_{\text{late}}^{\text{A,B}}$ and 35.2 cm is the distance from the center of the cylinder to the front face of the PMT.

The time between leading edges δt for the two PMTs is found. All data (PSD and neutron-source data, dis-

cussed later) are passed through a cut requiring $|\delta t| < 20$ ns. The average leading edge time of the two PMTs t_{edge} is used in PSD data to define a time window in software for accepting events in DEAP-1 with respect to the time of the back-PMT signal. For PSD data, a cut is imposed that accepts only events whose leading edge time is within 30 ns of the mean time as found by a Gaussian fit to the distribution. This cut reduces random pileup of calibration γ rays with high- F_{prompt} backgrounds, described later. Figure 4 shows the timing distributions for a typical PSD run.

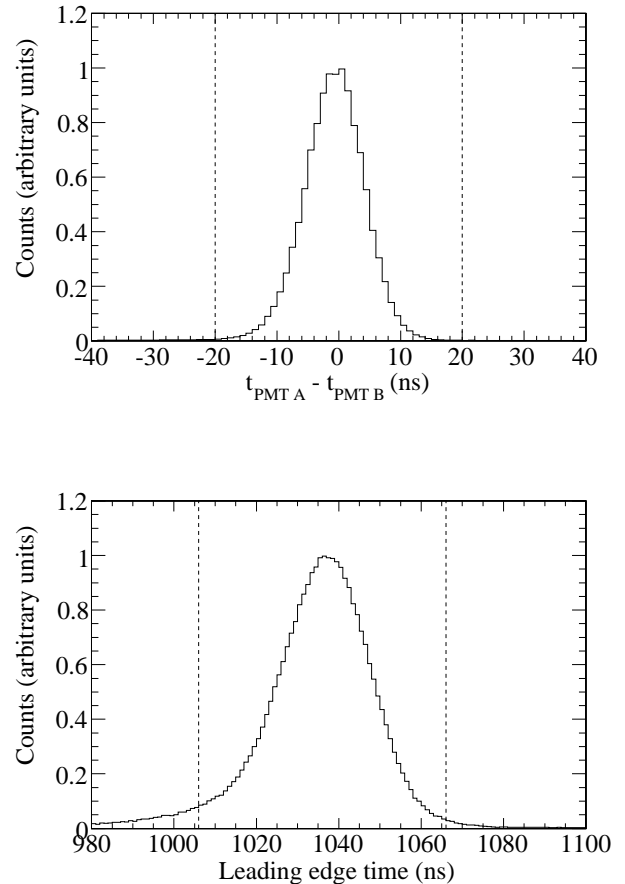


FIG. 4: The timing distributions for a typical run. The vertical lines indicate the cut values. For the top plot the cuts are always imposed at ± 20 ns. For the bottom plot the mean value is determined by a Gaussian fit and the cuts are imposed at the mean ± 30 ns.

The mean charge from single photoelectrons (spe) is derived from these data. Using only pulses with a low number of photoelectrons (below 200), we scan the final 4 μs of the pulses (high-gain channel only) looking for signals crossing a threshold of 5 mV. These signals are integrated from 5 ns before the threshold crossing to 20

ns after the threshold crossing (a total of 26 samples). On a run-by-run basis these spe charges are collected in a histogram. The mean charge is determined by the iterative procedure outlined in Ref. [11] that finds the mean between 0.4 and 2.5 times the previous value until convergence is achieved. Figure 5 shows histograms for a typical run. The mean charges for the two PMTs are 1.73 and 1.82 pC, with a variation throughout the running period of less than 4%.

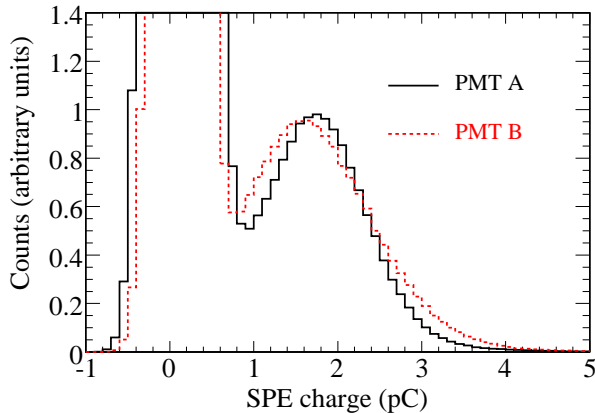


FIG. 5: Single photoelectron spectra of the DEAP-1 PMTs, used to calibrate the absolute light yield and number of detected photons.

The energy response is calibrated throughout the data taking with the full-energy peak from ^{22}Na . The light yield is approximately 2.8 ± 0.1 photoelectrons/ keV_{ee} (see Fig. 11) where keV_{ee} is the electron-equivalent energy, calibrated by the ^{22}Na peak. The light yield was stable throughout the 67-day running period.

IV. RESULTS

Data were collected with the DEAP-1 detector between August 20th and October 16th, 2007. A total of 63,072,900 triple-coincidence ^{22}Na calibration events were recorded for the PSD analysis. Figure 6 shows the distribution of F_{prompt} versus number of photoelectrons for these events; for this data set a hardware threshold imposed with the SCA restricts the high-photoelectron events to approximately 300 photoelectrons. Analysis of neutron calibration data shows that this does not remove high- F_{prompt} ($0.7 < F_{\text{prompt}} < 1$) nuclear recoil events. Figure 7 shows the F_{prompt} versus photoelectron distribution for neutrons and γ -rays from an Americium-Beryllium (Am-Be) calibration source. From these data we have evaluated the PSD in liquid argon and measured

parameters that can be used to describe the F_{prompt} distribution as a function of energy. As shown in Section V, we expect to use pulse-shape discrimination for signals of approximately 120 photoelectrons and above. We therefore pre-determined the region of interest for demonstration of PSD to be 120-240 photoelectrons, corresponding to approximately 43–86 keV_{ee} in DEAP-1. Figure 8 shows the F_{prompt} distribution for γ -rays and nuclear recoils, for events between 120 and 240 photoelectrons. We find that none of the 16.7 million γ -ray events leak into the nuclear recoil region, and infer that the PSD in liquid argon is less than 6×10^{-8} from these data. Table IV shows the mean F_{prompt} values and the inferred singlet/triplet ratios for electronic and nuclear recoil events versus energy in liquid argon.

We have also repeated this analysis with a lower photoelectron threshold and higher F_{prompt} region. For a neutron detection efficiency of 50%, there is one contamination event observed between 70–240 photoelectrons (approximately 25–86 keV_{ee}), for an observed pulse-shape discrimination of 4.7×10^{-8} in that range.

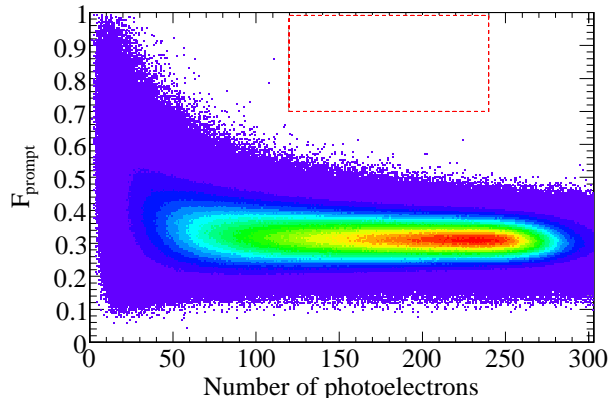


FIG. 6: F_{prompt} versus energy distribution for the triple-coincidence γ -ray events. The region between 120-240 photoelectrons for $F_{\text{prompt}} > 0.7$ contains no events.

Several tests of detector stability were performed. Impurities in the argon can decrease the light yield by absorbing UV photons or by quenching argon dimers before they decay, thereby also decreasing the observed lifetime of the triplet state in liquid argon [12, 13]. Therefore, we

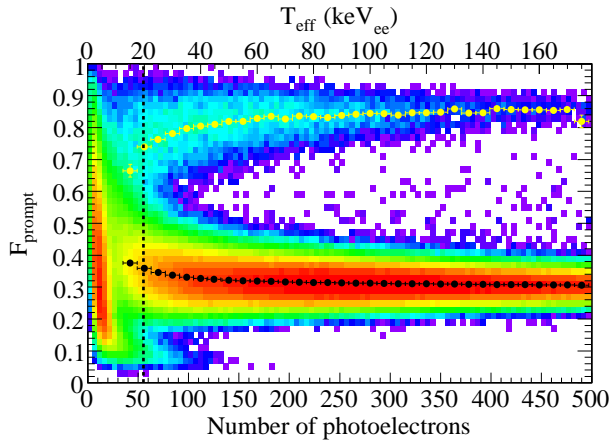


FIG. 7: F_{prompt} versus energy distribution for neutrons and γ rays from an Am-Be calibration source. The upper band is from neutron-induced nuclear recoils in argon, the lower band is from background γ -ray interactions.

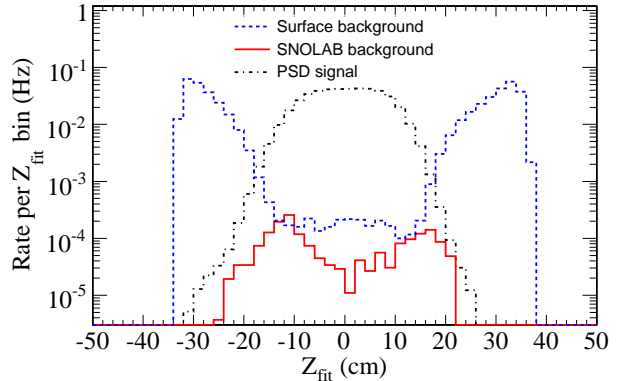


FIG. 9: Comparison of Z_{fit} distribution for γ -rays from the PSD data, and for high- F_{prompt} backgrounds during the run (labeled Surface backgrounds). Also shown, for reference, is the distribution of high- F_{prompt} background events with the detector operating underground at SNOLAB.

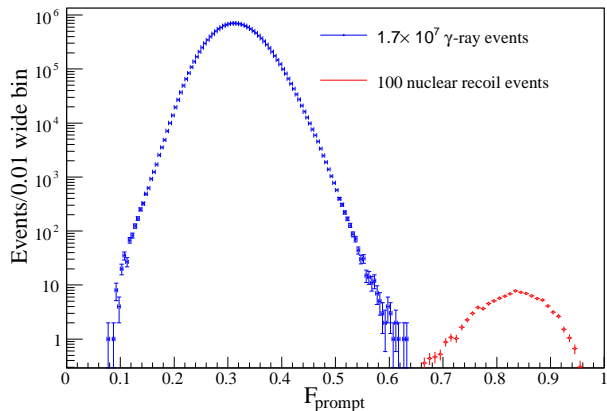


FIG. 8: F_{prompt} distribution for 16.7 million tagged γ -ray events from the ^{22}Na calibration, and nuclear recoil events from the Am-Be calibration, between 120 and 240 photoelectrons (approximately 43–86 keV_{ee}). No γ -ray events are seen in the nuclear recoil region.

measured the triplet lifetime in DEAP-1 over the course of the run to check that impurities did not build up in the detector over time.

We use ^{22}Na calibration data to measure the triplet lifetime. For each calibration run, we find all events that pass the data cleaning cuts and contain over 200 photoelectrons. The raw traces for these events are aligned according to the measured trigger positions and summed. We then fit the following model to the average trace between 500 and 3000 ns from the trigger:

$$f(t) = A \exp(-t/\tau_3) + B, \quad (3)$$

where A is a normalization factor, τ_3 is the triplet lifetime and B is a constant baseline term.

As a consistency check, we measured τ_3 for photoelectron bins of size 200 between 200 and 1600 photo-

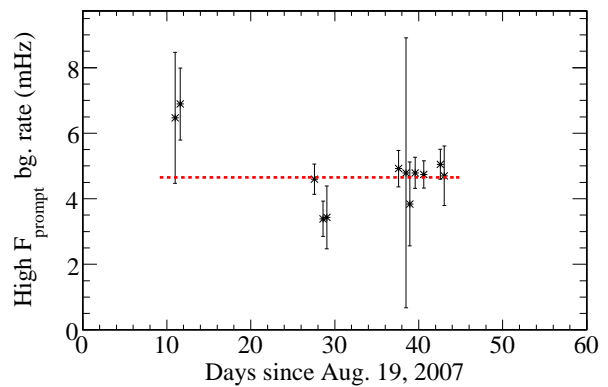


FIG. 10: High- F_{prompt} background event rate versus time. The average background rate is 4.6 ± 0.2 mHz.

electrons and did not observe any systematic effect from the signal size. There are systematic errors associated with both the fit window and the linear baseline correction discussed in Section III C. We estimated the size of the error associated with the fit window to be 40 ns by changing the start and end times of the fit by 500 ns. We performed the fit for both corrected and uncorrected traces and estimated the size of the error associated with the baseline to be 50 ns. We added the two estimated systematic errors to determine a combined systematic error of 60 ns.

The measured lifetimes over the course of the run for traces without the baseline correction are shown in Fig. 12, in which the error bars shown are statistical only. We observe no significant increase in the impurity level throughout the run, and we measure the long time constant to be 1.46 ± 0.06 (sys) μs , consistent with previous measurements [5, 13, 14]. Further analysis of systematic

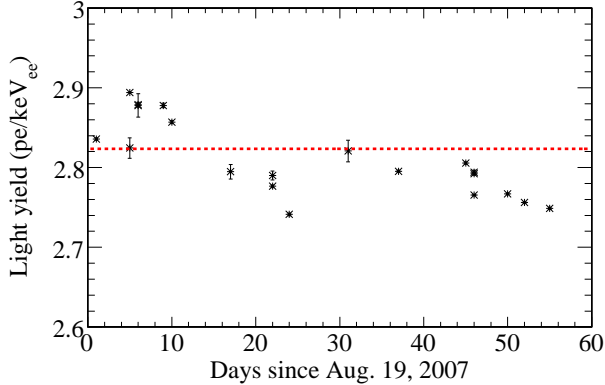


FIG. 11: Light yield stability during the run. The average light yield is 2.8 photoelectrons/keV_{ee}. Shown are statistical uncertainties only. The scatter of the data points is within the systematic uncertainty of the measurement.

uncertainties related to the fit window and baseline correction as well as hardware improvements and investigation of the effect on triplet lifetime of possible impurities in the argon are being investigated for the SNOLAB run.

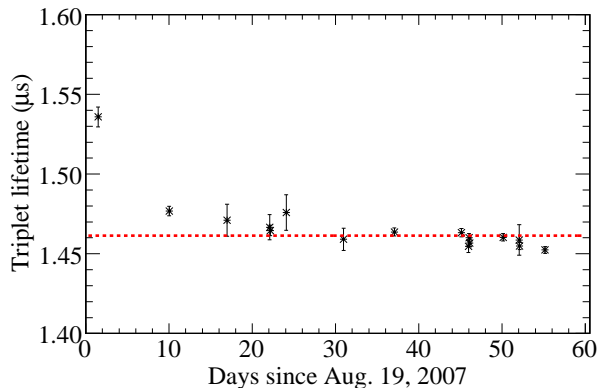


FIG. 12: Measured lifetime of the triplet component in liquid argon during the run. Uncertainties shown are statistical only. The scatter in the data points is consistent with the systematic uncertainty of the measurement. No significant change in the lifetime was seen.

High- F_{prompt} (nuclear recoil) backgrounds are evaluated using the DEAP-1 trigger without any calibration sources present. Figure 9 shows the Z_{fit} distribution of high- F_{prompt} background events, compared to that of ^{22}Na calibration γ -ray events. Also shown for reference is the Z_{fit} distribution of high- F_{prompt} background events with the DEAP-1 detector operating underground at SNOLAB. The reduced backgrounds underground will allow a more sensitive measurement of

TABLE I: Measured values of F_{prompt} and singlet/triplet intensity ratios (I_1/I_3) versus energy (T) for neutron-induced nuclear recoils and for electrons in liquid argon.

electron recoils			nuclear recoils		
T	F_{prompt}	I_1/I_3	T	F_{prompt}	I_1/I_3
(keV _{ee})			(keV _r)		
15	0.38	0.46	50	0.66	1.71
20	0.36	0.42	66	0.74	2.50
25	0.35	0.39	83	0.76	2.80
30	0.34	0.37	100	0.78	3.17
35	0.33	0.36	116	0.80	3.49
40	0.33	0.35	133	0.80	3.66
45	0.32	0.35	150	0.81	3.79
50	0.32	0.34	166	0.82	4.05
75	0.32	0.33	250	0.84	4.57
100	0.31	0.32	333	0.85	4.88
125	0.31	0.32	416	0.85	5.01
150	0.31	0.31	500	0.86	5.37
200	0.29	0.28	666	0.86	5.56

PSD in argon. The average background rate in the region of interest (120-240 photoelectrons) measured for the data presented in this paper is 4.6 ± 0.2 mHz, constant throughout the run as shown in Fig. 10.

With the triple-coincidence tag, the measurement on surface is limited by random coincidences between the global tag (back-PMT and annulus) and high- F_{prompt} background events in DEAP-1. The rate of high- F_{prompt} pile-up during the γ -ray calibration run is

$$R_{\text{bkg}} = R_{\text{tag}} R_n \Delta t, \quad (4)$$

where R_{tag} is the global tag rate, R_n is the rate of high- F_{prompt} background events measured in DEAP-1 and Δt is the width of the time window (applied with the software cut).

The achievable PSD can be found by dividing R_{bkg} by the rate of data acquisition in the energy region of interest (ROI), R_{ROI} :

$$D_{\text{bkg}} = \frac{R_{\text{bkg}}}{R_{\text{ROI}}} = \frac{R_{\text{tag}} R_n \Delta t}{R_{\text{ROI}}}. \quad (5)$$

D_{bkg} is thus the discrimination level where we would expect to find one background event. Table II shows the relevant parameters and the result from calculating D_{bkg} , and this background is below the demonstrated discrimination level of 6×10^{-8} .

It should be noted that the high- F_{prompt} background rate has been reduced by a factor of approximately 10 at SNOLAB, and further background reduction is expected, allowing for a more sensitive measurement of PSD in argon.

TABLE II: Background from random coincidence between the global tag and high- F_{prompt} background events in the argon. R_{tag} is the coincidence rate between the annulus and back-PMT with the ^{22}Na source in place, Δt is the coincidence time window imposed by the analysis, R_n is the rate of high- F_{prompt} background events in the liquid argon, R_{ROI} is the rate of triple-coincidence events and D_{bkg} is the PSD level where one radon-coincidence background event is expected.

Variable	Values
R_{tag} (Hz)	1000
Δt (ns)	60
R_n (mHz)	4.6
R_{ROI} (Hz)	18
D_{bkg}	1.53×10^{-8}

V. ANALYTIC MODEL FOR DISCRIMINATION POWER

We developed a model for the F_{prompt} distribution by assuming that the singlet and triplet contributions are both Gaussian and uncorrelated. The distribution of F_{prompt} values F_p is then a ratio of two Gaussian distributions, which to a good approximation can be written as [15]

$$P(F_p) = \frac{1}{\sqrt{2\pi}} \frac{\sigma_L^2 \mu_P + \sigma_P^2 \mu_L F_p}{(\sigma_L^2 + \sigma_P^2 F_p^2)^{3/2}} \times e^{-\frac{1}{2}(\mu_L - \mu_P F_p)^2 / (\sigma_L^2 + \sigma_P^2 F_p^2)} \quad (6)$$

The distribution is thus a function of four parameters: the means μ_P, μ_L and widths σ_P, σ_L of both the singlet (prompt light) and triplet (late light) distributions. Each of the four parameters depends on the event energy, and the ideal distribution in Eq. (6) has to be convolved with the energy response of the detector to adequately model the observed data.

By definition, the parameters μ_P, μ_L are functions of the most likely F_{prompt} value \bar{F}_p :

$$\mu_P = \bar{F}_p N_{pe} \quad (7)$$

and

$$\mu_L = (1 - \bar{F}_p) N_{pe} \quad (8)$$

so that their energy dependence is known if that of \bar{F}_p is known.

The energy dependence of the distribution widths σ_P, σ_L is modeled by splitting σ up into the following components: uncertainty in the single photoelectron calibration σ_{spe} , uncertainty in the counting window due to uncertainty in the trigger time σ_{win} , electronic noise σ_{elec} and statistical uncertainty σ_{stat} , so that

$$\sigma^2 = \sigma_{\text{stat}}^2 + \sigma_{\text{spe}}^2 + \sigma_{\text{elec}}^2 + \sigma_{\text{win}}^2. \quad (9)$$

Writing the statistical noise as the square root of the number of photoelectrons in the prompt or late window

we have

$$\sigma_{\text{stat,P}}^2 = \bar{F}_p N_{pe} \quad (10)$$

$$\sigma_{\text{stat,L}}^2 = (1 - \bar{F}_p) N_{pe}. \quad (11)$$

The single photoelectron noise contribution is then

$$\sigma_{\text{spe,P}} = (\sigma_{\text{spe}}^P / \mu_{\text{spe}}^P) \sqrt{\bar{F}_p N_{pe}} \quad (12)$$

$$\sigma_{\text{spe,L}} = (\sigma_{\text{spe}}^P / \mu_{\text{spe}}^P) \sqrt{(1 - \bar{F}_p) N_{pe}}, \quad (13)$$

where μ_{spe}^P and σ_{spe}^P are the mean and width of the single photoelectron peak.

The uncertainty in the counting window of approximately 30 ns leads to an uncertainty in the late photoelectron count of 2.5%. Electronic noise of 0.58 photoelectrons in the prompt window, and 3.7 photoelectrons in the late window are measured by triggering the detector with a pulser and analyzing the PMT traces. The fraction $\sigma_{\text{spe}}^P / \mu_{\text{spe}}^P$ is measured to be 0.276. The final expressions for the dependence of σ_P and σ_L on the number of photoelectrons, and thus on the energy of the event, are then

$$\sigma_P^2 = \bar{F}_p N_{pe} + (0.276 \sqrt{\bar{F}_p N_{pe}})^2 + (0.58 \text{ pe})^2 + (0.025(1 - \bar{F}_p) N_{pe})^2 \quad (14)$$

$$\sigma_L^2 = (1 - \bar{F}_p) N_{pe} + (0.276 \sqrt{(1 - \bar{F}_p) N_{pe}})^2 + (3.7 \text{ pe})^2 + (0.025(1 - \bar{F}_p) N_{pe})^2 \quad (15)$$

The behaviour of the prompt and late noise versus the number of photoelectrons is illustrated in Fig. 13 and Fig. 14.

Finally, since the F_{prompt} distribution depends on energy and number of photoelectrons, the distribution is convolved with the energy spectrum of interest $N(E)$:

$$P^*(F_p, N_{pe}) = \sum_{n=0}^{\infty} N(n) P(fp(n), n) \times \frac{1}{\sigma(n) \sqrt{2\pi}} e^{-\frac{(N_{pe} - n)^2}{2\sigma n^2}} \quad (16)$$

where the energy E has been converted to number of photoelectrons n and $\sigma(E)$ is the energy resolution function as determined from the detector's energy calibration. This model agrees with the data for energies above 60 photoelectrons. A comparison between the model and the data is shown in Fig. 15 for the energy region 60-120 photoelectrons, and in Fig. 16 for the energy region 120-240 photoelectrons. The dark gray line is from Eq. (16) and the shaded area represents the systematic uncertainty from uncertainties in energy calibration and noise parameters.

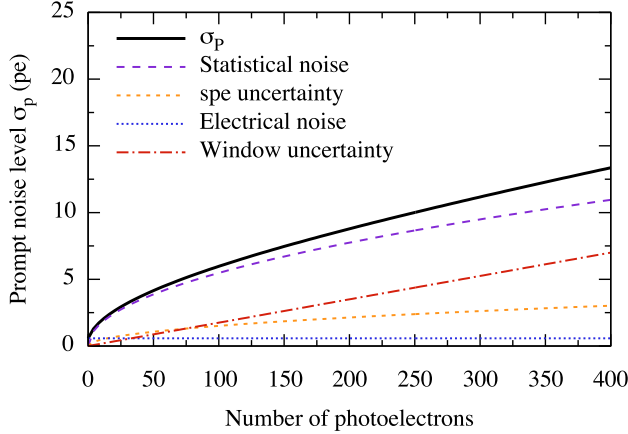


FIG. 13: The noise level σ_P in the prompt time window is shown as a function of the total number of photoelectrons in the pulse. The broken lines show how the four sources of noise and uncertainty that are taken into account in our model contribute to the total noise level.

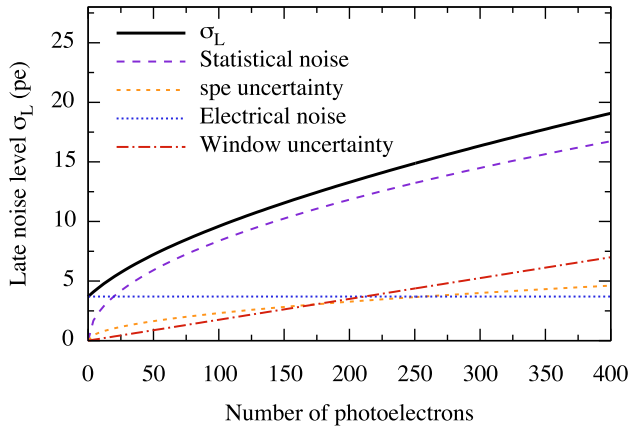


FIG. 14: The noise level σ_L in the late time window is shown as a function of the total number of photoelectrons in the pulse. The broken lines show how the four sources of noise and uncertainty that are taken into account in our model contribute to the total noise level.

To represent the discrimination power graphically, we define the variable P_{leak} as

$$P_{\text{leak}}(F') = \frac{\int_0^{F'} F_{\text{prompt}}(x) dx}{\int_0^1 F_{\text{prompt}}(x) dx} \quad (17)$$

for a given F_{prompt} distribution. The value of P_{leak} for a given F_{prompt} value thus represents the pulse-shape discrimination. Figure 17 shows the P_{leak} distribution derived from the ^{22}Na calibration data, along with the predictions from the analytic PSD model. Also shown are the analytic model assuming that the systematic noise

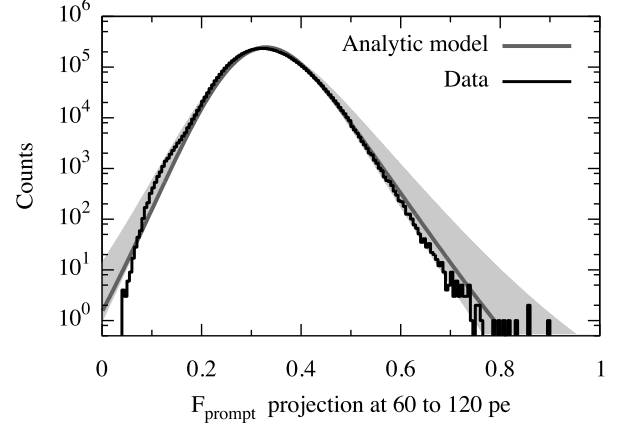


FIG. 15: Comparison of the data and the analytic model in the region 60-120 photoelectrons (approximately 21–43 keV_{ee}). The gray shaded area represents the uncertainty in the noise parameters and in the energy calibration.

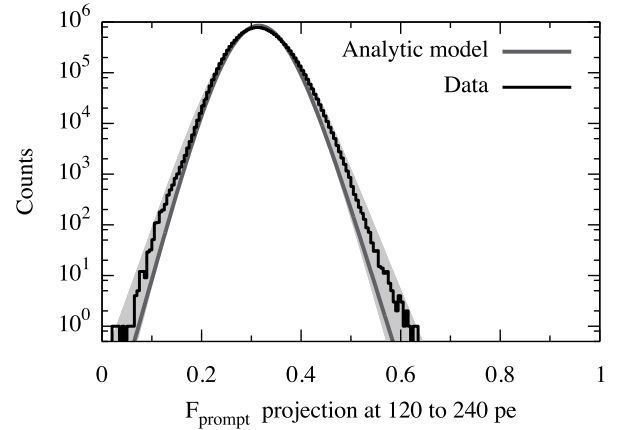


FIG. 16: Comparison of the data and the analytic model in the region 120-240 photoelectrons (approximately 43–86 keV_{ee}). The gray shaded area represents the uncertainty in the noise parameters and in the energy calibration.

parameters are negligible, the acceptance for nuclear recoil events, and the limit expected from surface background contamination.

VI. DARK MATTER SENSITIVITY

Using Eq. (16) we next evaluate the expected discrimination power in liquid argon versus energy threshold assuming a large target mass detector. We have designed DEAP-3600, a large spherical detector consisting of approximately 250 PMTs surrounding a spherical target with a mass of 3600 kg of liquid argon. Geant4 simulations benchmarked against the light yield in the DEAP-1 detector predict that in this geometry a light yield of approximately 6 photoelectrons/ keV_{ee} could be achieved.

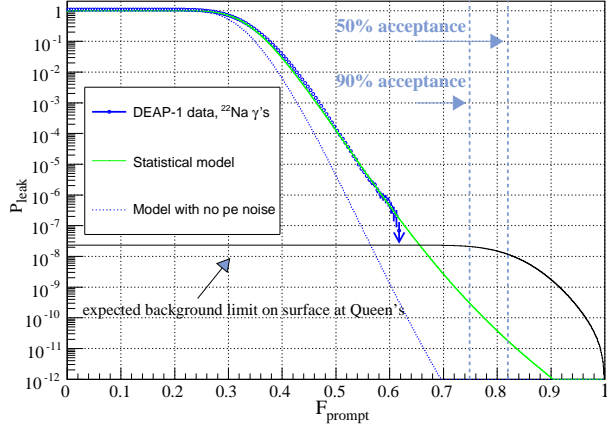


FIG. 17: P_{leak} distribution from ^{22}Na calibration data from DEAP-1, and analytic models with and without additional noise parameters for 120–240 photoelectrons. The lower curve shows the expected backgrounds in the measurements from high- F_{prompt} events.

Assuming the detector is constructed of clean materials and appropriately shielded so that genuine nuclear recoil backgrounds have been mitigated, the dominant detector background in argon will be from β decays of ^{39}Ar . Argon that is condensed from the atmosphere is known to contain cosmogenically-produced ^{39}Ar , with a rate of decays of approximately 1 Bq per kg [16]. Recent work has shown that there is a possibility of obtaining argon that has been sequestered underground that is depleted in ^{39}Ar by a factor of 20 [17]. An optimization analysis has shown that we could achieve an analysis threshold of approximately 20 keV_{ee} for a dark matter particle search with natural argon; from Eq. (16) the expected discrimination is 10^{-10} at that threshold, which is sufficient to reduce the backgrounds from atmospheric ^{39}Ar decay to less than 0.2 events in a three-year run with 1000 kg of liquid argon in the energy window from 20–30 keV_{ee} . In that analysis we have assumed that for the large detector, each of the approximately 250 PMTs would detect on average less than a single photoelectron, and thus that the systematic noise parameters can be reduced so that they are negligible compared to the statistical uncertainties in Eq. (9). The P_{leak} distribution given by Eq. (17) is shown in Fig. 18. Fig. 19 shows the 90% confidence level sensitivity versus WIMP mass for both cases, compared to the current experimental limits of the CDMS [18] and XENON-10 [19] experiments. We have used standard assumptions for the galactic halo outlined in reference [20] and assumed a nuclear recoil scintillation efficiency of 30% compared to electrons [21].

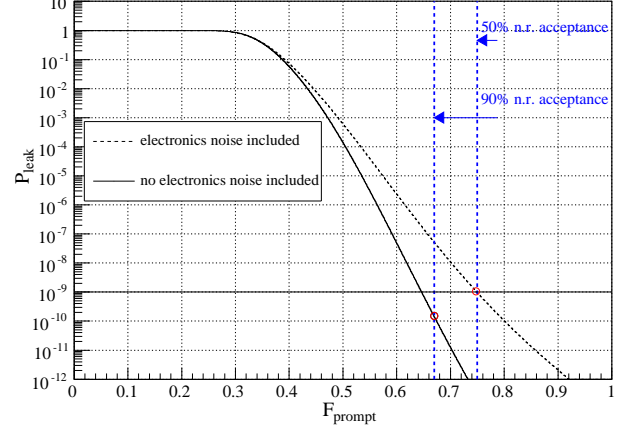


FIG. 18: P_{leak} distribution expected for 20–40 keV_{ee} with 6 photoelectrons/ keV_{ee} yield. Shown are the distributions with and without systematic noise terms, and the F_{prompt} values for 50% and 90% nuclear recoil acceptance.

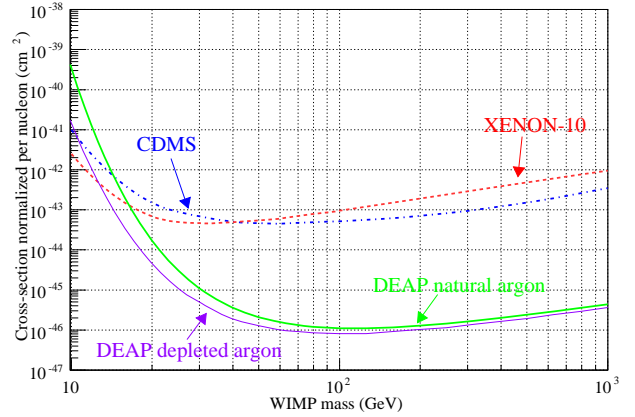


FIG. 19: Dark matter sensitivity of liquid argon. Shown are the current experimental limits from the CDMS and XENON-10 collaborations, and the expected sensitivity for 1000 kg of liquid argon with a 20 keV_{ee} threshold, and with a 19 keV_{ee} threshold for argon that has been depleted in ^{39}Ar by a factor of 20.

VII. SUMMARY

We have shown that pulse-shape discrimination in liquid argon can be used to separate γ -ray and nuclear recoil events in the energy region 43–86 keV_{ee} with a leakage of less than 6×10^{-8} for full recoil detection efficiency, and in the energy region of approximately 25–86 keV_{ee} with a leakage of less than 4.7×10^{-8} for a 50% recoil detection efficiency. An analytic model which assumes simple Gaussian distributions for the singlet and triplet components of the scintillation signal and accounts for statistical and systematic sources of noise in these distributions agrees with these data for events above 21 keV_{ee} . This model projects that available discrimination power in argon is 10^{-10} at 20 keV_{ee} , for a de-

detector with 6 photoelectrons/keV_{ee} light yield, allowing for sufficient background rejection of ³⁹Ar in a 1000-kg liquid argon dark matter experiment.

This work is supported by the National Science and

Engineering Research Council of Canada (NSERC), by the Canada Foundation for Innovation (CFI), by the Ontario Ministry of Research and Innovation (MRI), and by the David and Lucille Packard Foundation.

-
- [1] M. Boulay and A. Hime, *Astroparticle Physics* **25**, 179 (2006).
 - [2] M. Miyajima et al., *Phys. Rev.* **A9**, 1438 (1974).
 - [3] R. S. Mulliken, *J. Chem. Phys.* **52** (1970).
 - [4] A. Gedanken et al., *J. Chem. Phys.* **57** (1972).
 - [5] A. Hitachi and T. Takahashi, *Physical Review B* **27**, 5279 (1983).
 - [6] SAES PS4-MTR-3-R1 getter specifications, <http://www.saesgetter.com>.
 - [7] S. Agostinelli and Others, *Nuclear Instruments and Methods in Physics Research A* **506**, 250 (2003).
 - [8] J. Allison et al., *IEEE Transactions on Nuclear Science* **53**, 270 (2006).
 - [9] R. Brun and F. Rademakers, *Nuclear Instruments and Methods in Physics Research A* **389**, 81 (1997).
 - [10] High Performance Computing Virtual Laboratory, <http://www.hpcvl.org>.
 - [11] C. Jillings et al., *Nuclear Instruments and Methods in Physics Research A* **373**, 421 (1996).
 - [12] R. Acciarri et al. (WArP) (2008), e-print arXiv.org/0804.1222.
 - [13] R. Acciarri et al. (WArP) (2008), 0804.1217.
 - [14] W. H. Lippincott et al., *Phys. Rev.* **C78**, 035801 (2008), e-print arXiv.org/0801.1531.
 - [15] D. V. Hinkley, *Biometrika* **56**, 635 (1969).
 - [16] H. H. Loosli, *Earth and planetary science letters* **63**, 51 (1983).
 - [17] D. Acosta-Kane et al., *Nucl. Instrum. Meth. A.* **587**, 46 (2008).
 - [18] CDMS collaboration, *Phys. Rev. Lett.* **96**, 011302 (2006).
 - [19] J. Angle et al., *Phys. Rev. Lett.* **100**, 021303 (2008).
 - [20] J. D. Lewin and P. F. Smith, *Astropart. Phys.* **6**, 87 (1996).
 - [21] D. Gastler et al. (2009), to be published.